Accepted Manuscript

Title: Plasma Catalytic Steam Methane Reforming for Distributed Hydrogen Production

Authors: Xiaobing Zhu, Xiaoyu Liu, Hao-Yu Lian, Jing-Lin Liu, Xiao-Song Li

PII: S0920-5861(19)30232-9
DOI: https://doi.org/10.1016/j.cattod.2019.05.015
Reference: CATTOD 12191

To appear in: *Catalysis Today*

Received date: 23 January 2019
Revised date: 14 April 2019
Accepted date: 7 May 2019

Please cite this article as: Zhu X, Liu X, Lian H-Yu, Liu J-Lin, Li X-Song, Plasma Catalytic Steam Methane Reforming for Distributed Hydrogen Production, *Catalysis Today* (2019), https://doi.org/10.1016/j.cattod.2019.05.015

Plasma Catalytic Steam Methane Reforming for Distributed Hydrogen Production

Xiaobing Zhu, Xiaoyu Liu, Hao-Yu Lian, Jing-Lin Liu, Xiao-Song Li**

Center for Hydrogen Energy and Environmental Catalysis, Dalian University of Technology, Dalian 116024, China.

* Corresponding authors. Email: xzhu@dlut.edu.cn (X.Z.), lixsong@dlut.edu.cn (X.L.)

Graphical abstract

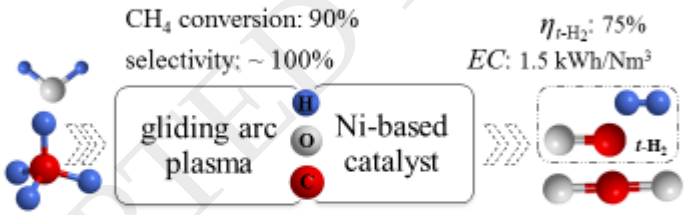

Highlights:

- Warm plasma catalytic steam methane reforming (SMR) for distributed hydrogen production is demonstrated.
- The methane conversion of 90% is achieved at total hydrogen (t-H_2) production rate of 2.7 SLM.
- The energy efficiency (of CH_4 to t-H_2) of 75% and the low energy cost of 1.5 kWh/Nm^3 is achieved.
- The formation of C_2H_x can be suppressed by *SEI* and *S/C* at plasma zone, and completely dismissed at catalyst bed zone.

ABSTRACT

Steam methane reforming (SMR) via thermal catalytic approach is one of the dominant sources of industrial hydrogen, however it proceeds with slow response and low specific productivity. Here we demonstrate a plasma catalytic SMR for distributed hydrogen production, for which warm plasma by gliding arc discharge initiates the reaction, followed by Ni-based catalyst in a heat-insulated reactor without extra heating. In terms of the plasma alone process, specific energy input (*SEI*), steam/CH_4 ratio (*S/C*) and total inlet flow rate (F_t) contribute to the methane conversion. In parallel, *SEI* and *S/C* account for the decrease in C_2H_x selectivity hence the increase in selectivity of CO and CO_2, while with F_t all the selectivity is approximately constant. The reaction pathway represented by the selectivity can be influenced by *SEI* and *S/C* rather F_t. To utilize the heat and active species with the reaction in plasma zone, $Ni/CeO_2/Al_2O_3$ catalyst bed is coupled. For the coupled process, the conversion approaches the thermodynamic equilibrium values, with the favorable dismissed C_2H_x selectivity thus the complete selectivity to CO and CO_2. The coupled process was maintained steady for six hours, and the methane conversion of 90% at total hydrogen (t-H_2) production rate of 2.7 SLM is achieved under optimum conditions of *SEI*, S/C, F_t and gas hourly space velocity (GHSV) of 110 kJ/mol, 3, 3 SLM and 18000 $ml \cdot g^{-1} \cdot h^{-1}$. Compared to 59% and 2.3 kWh/Nm^3 of the plasma alone process, such a coupled process achieves the energy efficiency (of methane to t-H_2) of 75% and the low energy cost of 1.5 kWh/Nm^3. Consequently, our approach of plasma catalytic SMR features the merits of rapid response, compact system and high specific productivity, which can be anticipated for the emerging needs of distributed hydrogen generation.

KEYWORDS: hydrogen production; steam methane reforming; plasma catalysis; gliding arc

1. INTRODUCTION

Hydrogen energy in combination with fuel cell electric vehicles (FCEVs) can be well deployed when the safety concern on the use of hydrogen and the on-demand accessibility are fully addressed.

Distributed hydrogen production is crucial to address (to minimize) the safety issue related to hydrogen storage and delivery. Currently, the blooming establishment of hydrogen station in California, U.S. (35 open and 29 in development) is a sign for the needs of distributed hydrogen production [1].

Fossil fuels are the dominant sources of industrial hydrogen. Recently, methane reforming for hydrogen production has been intensively investigated due to the abundance, ease of liquefaction, the highest hydrogen storage capacity (i.e., hydrogen/carbon ratio), and no carbon-carbon bond [2-6]. Steam methane reforming (SMR) reaction (R1) possesses theoretically the largest mole fraction of hydrogen in product gas, compared with partial oxidation [7]and autothermal reforming [8].

$$\mathrm{CH_4 + H_2O \rightarrow 3H_2 + CO} \quad \Delta H^{\ominus}_{298.15\,K} = 206\ \mathrm{kJ/mol} \tag{R1}$$

Thermocatatlytic approach for SMR for industrial hydrogen production exhibits high selectivity of target product [9, 10]. Of strong endothermic reaction, thermocatalytic SMR occurs with necessary external heat supply, and thus large volumeric size and slow response, for which it is usually conducted for continuous stationary production of hydrogen at large scale.

Non-thermal plasmas [11], e.g., cold plasma and warm plasma, possess the merits of compact, rapid response, which can be suitable for distributed hydrogen production at small scale. In terms of the rate and efficiency of hydrogen production, the cold plasmas including dielectric barrier discharge (DBD) [12-15] and corona discharge [16], are far inferior to the warm plasmas represented by microwave discharge [17-19] and gliding arc discharge [20-26]. As a consequence, the warm plasma for methane reforming is a very active subject [17-19, 23, 26]. Ni-based catalyst of a recognized industrial catalyst exhibits high catalytic performance with low cost [27-29]. So far, no such a work on the SMR using (gliding arc) plasma catalytic approach is reported.

In the present work, the plasma catalytic SMR for distributed hydrogen production is performed, for which warm plasma by gliding arc discharge initiates the reaction, followed by Ni-based ($Ni/CeO_2/Al_2O_3$) catalyst in a heat-insulated reactor without extra heating. Under the optimal conditions of plasma alone process, the coupled process performs well in terms of conversion, selectivity and efficiency. The catalyst before and after stability test is observed by techniques of X-ray diffraction (XRD)

and X-ray photoelectron spectroscopy (XPS), scanning electron microscopy (SEM) and energy-dispersive X-ray spectroscopy (EDS).

2. EXPERIMENTAL PROCEDURES

As described in our previous work [30], the experimental setup is shown in Figure S1. After vaporization, a gas mixture of steam and methane (99.999% purity) is fed into a stainless steel reactor, which is insulated by ceramic fiber cotton. An input of DC power is applied for the generation of gliding arc discharge at atmospheric pressure. For gliding arc discharge, the discharge current (*I*) equals the output current of the power supply, which is measured by a built-in ampere meter. The discharge voltage (*U*) is equal to the voltage of the current limiting resistance subtracted from the output voltage of the DC power. The plasma power (*P*) is obtained by the product of discharge voltage and discharge current.

Catalyst is packed and located at post plasma zone in the reactor if applicable. Ten grams catalyst (3.5 cm height) is set at gas hourly space velocity (GHSV) of 18000 $ml \cdot g^{-1} \cdot h^{-1}$ after plasma zone. A gap of 4 cm between high voltage electrode and the entry of catalyst bed is set. The axial temperature profile of central catalyst bed in the reactor and the reactor wall is measured using two thermocouples. By incipient wetness impregnation method, the precursors of aqueous $Ce(NO_3)_3$ and $Ni(NO_3)_2$ are subsequently dispersed with γ-Al_2O_3 support (1-2.5 mm in diameter) for overnight, followed by drying at 110 ^oC for 6 h and 500 ^oC for 6 h. The catalyst of $Ni/CeO_2/Al_2O_3$ with the loading of 11 wt.% Ni and 8 wt.% Ce is achieved.

As shown in Figure S1, two gas chromatographs (GC) are used in sequence, to analyze gasous product. For the accuracy, internal standard gas comes with sample gas. Specifically, helium gas as internal standard gas is used to quantify H_2, and nitrogen as internal standard gas for CH_4, CO, CO_2, C_2H_x hydrocarbon. The first GC (Agilent 1790T) consists of a thermal conductivity detector (TCD) and a TDX-01 column (2 mm inner diameter, 1.5 m length), which uses H_2 as carrier gas to quantitatively determine CH_4, CO, CO_2. The second GC (Agilent 6890N) consists of a TCD unit (with a column of carbon molecular sieve 601), and a flame ionization detector (FID) unit (with a porapak-N column),

which uses nitrogen as carrier gas. The TCD unit is used to detect H_2, and the FID unit is conducted for analysis of hydrocarbons, e.g., CH_4 and C_2H_x (C_2H_2, C_2H_4 and C_2H_6). The C_2H_x hydrocarbon is quantified based on the molar ratio of C_2H_x/CH_4, for which CH_4 is measured by the first GC. Using Gibbs free energy minimization by HSC Chemistry 7.0 software the thermodynamic equilibrium value (e.g., conversion) is calculated.

Conversion of CH_4 ($X_{\mathrm{CH_4}}$) and H_2O ($X_{\mathrm{H_2O}}$) is calculated using equations E1-E3,

$$X_{\mathrm{CH_4}} = \frac{F_{\mathrm{CH_4}}^{in} - F_{\mathrm{CH_4}}^{out}}{F_{\mathrm{CH_4}}^{in}} \times 100\% \tag{E1}$$

$$X_{\mathrm{H_2O}} = \frac{F_{\mathrm{H_2O}}^{in} - F_{\mathrm{H_2O}}^{out}}{F_{\mathrm{H_2O}}^{in}} \times 100\% \tag{E2}$$

$$F_{\mathrm{H_2O}}^{out} = F_{\mathrm{H_2O}}^{in} - F_{\mathrm{CO}}^{out} - 2F_{\mathrm{CO_2}}^{out} \tag{E3}$$

where F_{i}^{in} and F_{i}^{out} (Subscript i = CH_4, H_2O, CO, CO_2) represent the gaseous inlet and outlet flow rates, respectively.

Selectivity and balance is calculated on the basis of carbon atom or hydrogen atom. For the carbon-based, the selectivity of CO (S_{CO}), CO_2 ($S_{\mathrm{CO_2}}$) and C_2H_x ($S_{\mathrm{C_2}}^{C}$) and the carbon balance (B_{C}) are calculated using equations E4-E7,

$$S_{\mathrm{CO}} = \frac{F_{\mathrm{CO}}^{out}}{F_{\mathrm{CH_4}}^{in} \cdot X_{\mathrm{CH_4}}} \times 100\% \tag{E4}$$

$$S_{\mathrm{CO_2}} = \frac{F_{\mathrm{CO_2}}^{out}}{F_{\mathrm{CH_4}}^{in} \cdot X_{\mathrm{CH_4}}} \times 100\% \tag{E5}$$

$$S_{\mathrm{C_2}}^{C} = \frac{2(F_{\mathrm{C_2H_2}}^{out} + F_{\mathrm{C_2H_4}}^{out} + F_{\mathrm{C_2H_6}}^{out})}{F_{\mathrm{CH_4}}^{in} \cdot X_{\mathrm{CH_4}}} \times 100\% \tag{E6}$$

$$B_{\mathrm{C}} = S_{\mathrm{CO}} + S_{\mathrm{CO_2}} + S_{\mathrm{C_2}}^{C} \tag{E7}$$

where F_{i}^{out} (i = C_2H_2, C_2H_4, C_2H_6) denotes the gaseous outlet flow rate of C_2H_x. For the hydrogen-based, the selectivity of H_2 ($S_{\mathrm{H_2}}$) and C_2H_x ($S_{\mathrm{C_2}}^{H}$), and the hydrogen balance (B_{H}), are calculated using equations E8-E10,

$$S_{\mathrm{H_2}} = \frac{F_{\mathrm{H_2}}^{out}}{2F_{\mathrm{CH_4}}^{in} \cdot X_{\mathrm{CH_4}} + F_{\mathrm{H_2O}}^{in} \cdot X_{\mathrm{H_2O}}} \times 100\% \tag{E8}$$

$$S_{C_2}^{H} = \frac{2F_{C_2H_2}^{out}+4F_{C_2H_4}^{out}+6F_{C_2H_6}^{out}}{4F_{CH_4}^{in}\cdot X_{CH_4}+2F_{H_2O}^{in}\cdot X_{H_2O}} \times 100\% \quad \text{(E9)}$$

$$B_{H} = S_{H_2} + S_{C_2}^{H} \quad \text{(E10)}$$

where $F_{H_2}^{out}$ denotes the outlet flow rate of H_2.

The exothermicity of water-gas shift (WGS) reaction allows CO (with H_2O) converted to CO_2 and H_2 but without any extra energy input. Hence, the converted H_2 (from CO via WGS), would be counted to the present H_2, for which the sum of the present CO (representing the converted H_2) and the present H_2 is called total H_2 (*t*-H_2).

From methane to total H_2 (*t*-H_2), the energy efficiency (η) of and the energy cost (*EC*) are calculated according to equations E11-E12,

$$\eta = \frac{\left(F_{H_2}^{out}+F_{CO}^{out}\right)\cdot LHV_{H_2}}{F_{CH_4}^{in}\cdot X_{CH_4}\cdot LHV_{CH_4}+P} \times 100\% \quad \text{(E11)}$$

$$EC = \frac{P}{F_{H_2}^{out}+F_{CO}^{out}} \quad \text{(E12)}$$

where P represents plasma power, and LHV_{H_2}, LHV_{CH_4} for the lower heating values of H_2, CH_4, respectively.

For the product, dry-basis concentration of H_2 ($C_{H_2}^{dry}$), CO (C_{CO}^{dry}), *t*-H_2 ($C_{t-H_2}^{dry}$) is calculated using equations E13-E15,

$$C_{H_2}^{dry} = \frac{F_{H_2}^{out}}{F_{H_2}^{out}+F_{CH_4}^{out}+F_{CO}^{out}+F_{CO_2}^{out}+F_{C_2H_2}^{out}+F_{C_2H_4}^{out}+F_{C_2H_6}^{out}} \times 100\% \quad \text{(E13)}$$

$$C_{CO}^{dry} = \frac{F_{CO}^{out}}{F_{H_2}^{out}+F_{CH_4}^{out}+F_{CO}^{out}+F_{CO_2}^{out}+F_{C_2H_2}^{out}+F_{C_2H_4}^{out}+F_{C_2H_6}^{out}} \times 100\% \quad \text{(E14)}$$

$$C_{t-H_2}^{dry} = \frac{F_{H_2}^{out}+F_{CO}^{out}}{F_{H_2}^{out}+F_{CH_4}^{out}+2F_{CO}^{out}+F_{CO_2}^{out}+F_{C_2H_2}^{out}+F_{C_2H_4}^{out}+F_{C_2H_6}^{out}} \times 100\% \quad \text{(E15)}$$

X-ray diffraction (XRD) measurement on the catalysts before and after six-hour stability test is conducted by an X-ray diffractometer (XRD-6000, Rigaku Smartlab 9) using a Cu Kα radiation (λ=1.54 Å) at 45 kV and 200 mA in the 2θ ranging from 10° to 80° at 6°/min. X-ray photoelectron spectroscopy (XPS, ESCALAB 250Xi, Thermofisher, U.S.) measurement on the catalysts before and after the stabil-

ity test, is conducted using an Al Kα X-ray source (1486.6 eV) operated at 15 kV and 10.8 mA. The binding energy is calibrated according to the XPS peak of carbon 1s at 284.6 eV. Energy dispersive X-ray spectroscopy (EDS) for the observation of element mapping of the catalyst before and after stability test, is carried out on EDAX (AMETEK, U.S.).

Supporting Information describes experimental setup (Figure S1), stability test (Figure S2), and morphology and element mapping (Figure S3).

3. RESULTS AND DISCUSSION

For the plasma alone process, the effects of energy density (*SEI*), steam/CH_4 (*S/C*) ratio and total inlet flow rate (F_t) on SMR reaction were examined. The experimental conditions are listed in Table 1. With the reaction by plasma, the heat and the active species can be efficiently utilized by the subsequent catalyst, for which our warm plasma catalytic SMR was developed and performed well. The stability test was conducted, followed by the observations on the catalysts before and after the stability by XRD, XPS, and EDS. The energy efficiency and energy cost was analyzed compared to various plasma-related approaches.

Table 1. Experimental conditions for SMR in plasma zone.

Experiments	*SEI* / kJ/mol	S/C ratio	F_t / SLM	*I* / mA	*U* / kV	*P* / W
SEI effect	80-110	2.0	2.5	53-77	2.8-2.7	149-206
S/C effect	100	1.5-3.0	2.5	75	2.5	187
F_t effect	110	2.0	2.2-3.0	73-95	2.6	188-244

3.1 Gliding arc plasma

3.1.1 Energy density

With the increase in *SEI*, the formation of C_2H_x hydrocarbon (that may cause coking) is suppressed thus favorably the selectivity is enhanced. *SEI* contributes to the endothermic SMR reaction (R1), however not much to water-gas shift (WGS, R2) reaction due to its exothermicity. The gaseous product consists of mostly CO and H_2, with small amount of CO_2 and C_2H_x (mainly C_2H_2).

$$CO + H_2O \rightarrow H_2 + CO_2 \quad \Delta H^{\ominus}_{298.15\,K} = -41\ \mathrm{kJ/mol} \tag{R2}$$

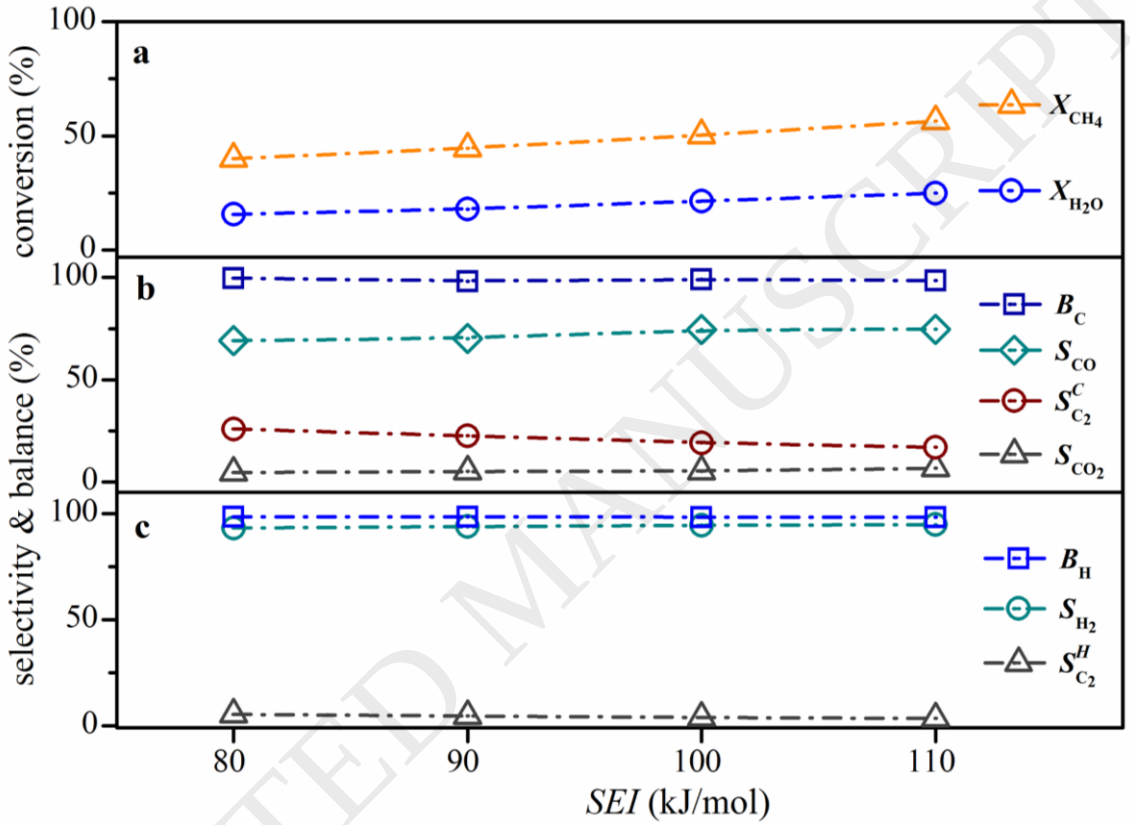

Figure 1. Effect of energy density, *SEI*, for SMR by warm plasma on (a) conversion, (b) carbon-based selectivity and balance and (c) hydrogen-based selectivity and balance, under conditions of total flow rate F_t of 2.5 SLM, and steam/methane (*S*/*C*) ratio of 2. The energy density of plasma, represented by *SEI*, equals the plasma power over the moles of reactant molecules.

In Figure 1a, with *SEI*, the methane conversion increases from 40% to 56% and water does from 15% to 24%, which is consistent with literatures [24, 31]. With this non-volumetric work (electric, comparable to heat), the thermodynamic equilibrium of endothermic SMR reaction shifts forward, hence with the increase in conversion. In Figures 1b and 1c, the mass balance of reaction is shown

approximate 100%(±3%). For the carbon-based selectivity, with *SEI* the decrease in C_2H_x (26 to 17%) approximately equals the increase in CO and CO_2 (69 to 74% and 4 to 7%), which exactly means the conversion of C_2H_x to CO and CO_2. With *SEI* the increase in CO selectivity is a little larger than that of CO_2. For the hydrogen-based selectivity, it has no obvious changes with *SEI* due to the very low concentration of C_2H_x in product gas. In Figure 1c, the hydrogen-based selectivity of C_2H_x drops 2% (from 5%) thus that of H_2 rises slightly 2% (to 95%).

3.1.2 S/C ratio

With S/C ratio the formation of C_2H_x is inhibited (thus the selectivity increases) and the WGS is promoted. Figure 2a shows that with the increase in S/C ratio from 1.5 to 3, the methane conversion increases from 46% to 55%, while the water conversion decreases from 27% to 17%. It is attributed to that the SMR reaction equilibrium shifts forward with the increase in water concentration of reactant. Figure 2b shows that under the approximate 100% (±3%) carbon balance, with S/C ratio the carbon-based selectivity of C_2H_x reduces from 20% to 13%, the CO_2 selectivity increases from 4% to 10%, and the CO selectivity keeps almost steady at 77%. The decrease in C_2H_x selectivity approximately equals the increase in CO_2 selectivity, while CO selectivity is constant. Interestingly, with the increase in S/C ratio, the CO selectivity increases because the SMR equilibrium shifts forward, however the CO conversion is enhanced since the WGS equilibrium shifts forward. Consequently, with S/C ratio the CO selectivity goes up for SMR (CO formation), and however the CO conversion rises for WGS (CO consumption), which results in the steady CO selectivity for the total reaction. As shown in Figure 2c, there is no obvious change in the hydrogen-based selectivity due to the very low concentration of C_2H_x in product gas, e.g., the selectivity of C_2H_x drops 2% (from 4%) thus that of H_2 rises slightly 2% (to 98%).

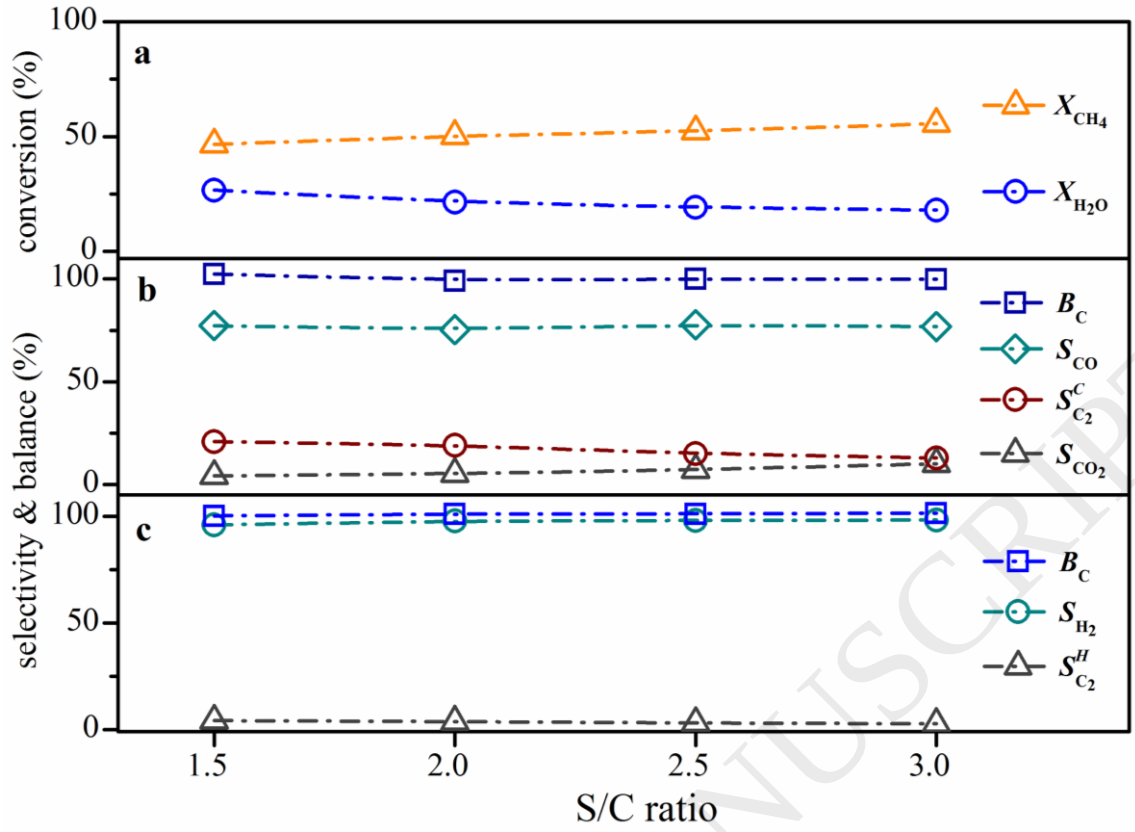

Figure 2. Effect of S/C ratio for SMR by warm plasma on (a) conversion, (b) carbon-based selectivity and balance and (c) hydrogen-based selectivity and balance, under conditions of total flow rate F_t of 2.5 SLM and *SEI* of 100 kJ/mol (the corresponding P^{in} of 188 W).

3.1.3 Total flow rate

Total flow rate, F_t contributes to the increase in methane conversion, however has no contribution on the inhibition of C_2H_x formation (thus no changes in the selectivity), indicating the identical reaction pathway (of methane reforming) herein. Figure 3a shows that with F_t from 2.2 to 3 SLM the methane conversion increases from 53% to 60% and that of water from 22% to 27%. Under conditions of the same *SEI* and S/C ratio, total flow rate does not influence the chemical equilibrium of SMR. Interestingly, with total flow rate the conversion of methane and water increases, which is attributed to the elongation of arc and the increase in rotation frequency of arc. In Figures 3b and 3c, the selectivity (of carbon-based and hydrogen-based) of CO, CO_2 and C_2H_x keeps basically constant with total flow rate.

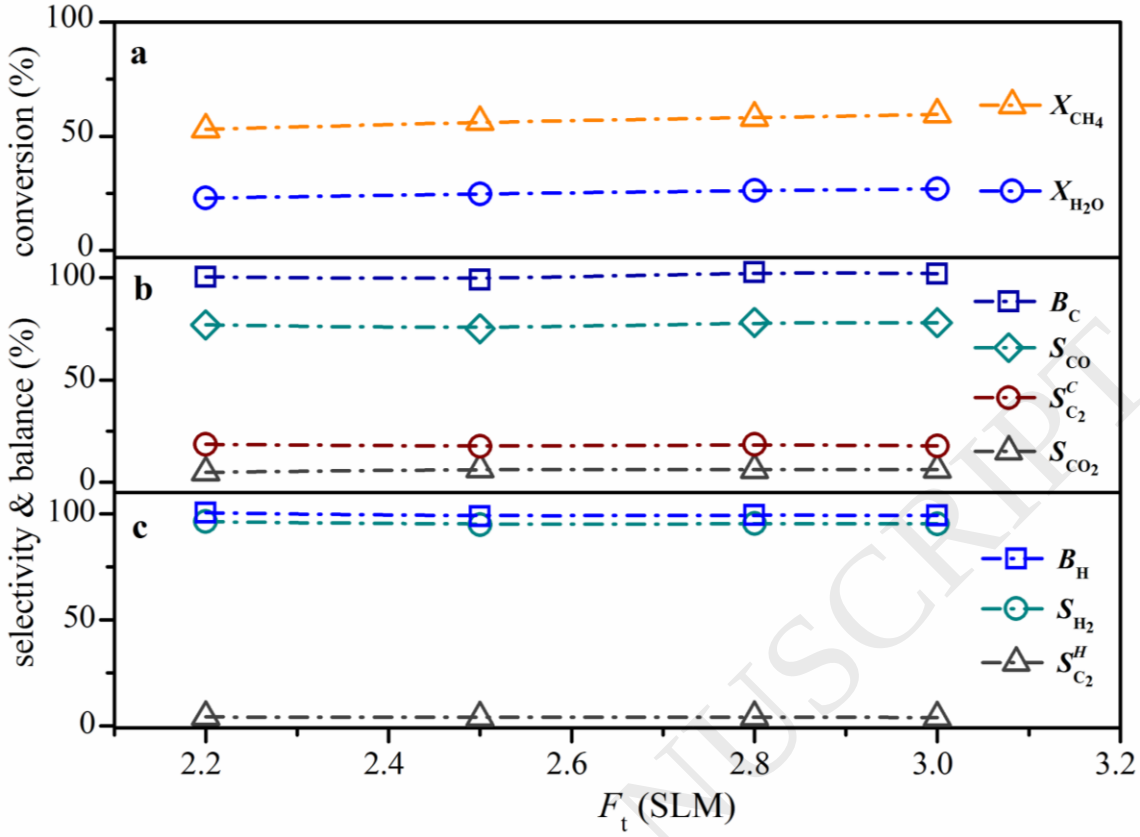

Figure 3. Effect of total inlet flow rate for SMR by warm plasma on (a) conversion, (b) carbon-based selectivity and balance and (c) hydrogen-based selectivity and balance, under conditions of *SEI* of 110 kJ/mol, S/C ratio of 2 (the corresponding *P* of 188-244 W).

So far, for the plasma alone process, two factors of *SEI* and *S/C* ratio contribute to the inhibition of C_2H_x formation (thus the increase in the selectivity), however F_t has no such contribution. In terms of methane conversion three factors of *SEI*, *S/C* ratio and F_t contribute. More interestingly, for the plasma catalytic process, the methane conversion is further enhanced favorably with the complete disappearance of C_2H_x.

3.2 Gliding arc plasma catalysis

For the plasma alone process, the stream remains high energy generated by gliding arc discharge (with the reaction). To efficiently utilize the heat and the active species sourced from the plasma zone, the catalyst bed is coupled subsequently. Since there is no extra heating and the only heat source from

the former plasma zone, the catalyst-bed temperature profile drops dramatically for the endothermicity of SMR reaction. Symbols T_c and T_w, and x_{CB} represent the axial temperature of catalyst bed and reactor wall, and the axial distance from the entry of the catalyst bed, respectively. In Figure 4a, the catalyst-bed temperature, T_c drops dramatically from 977 to 726 °C at the first 2 cm in catalyst-bed height, and slowly down to 651 °C at the end of catalyst bed. The temperature of reactor wall, T_w keeps steady at around 605 °C. For consistency, the end temperature of catalyst bed, 651 °C is set for that of thermodynamic equilibrium state for SMR.

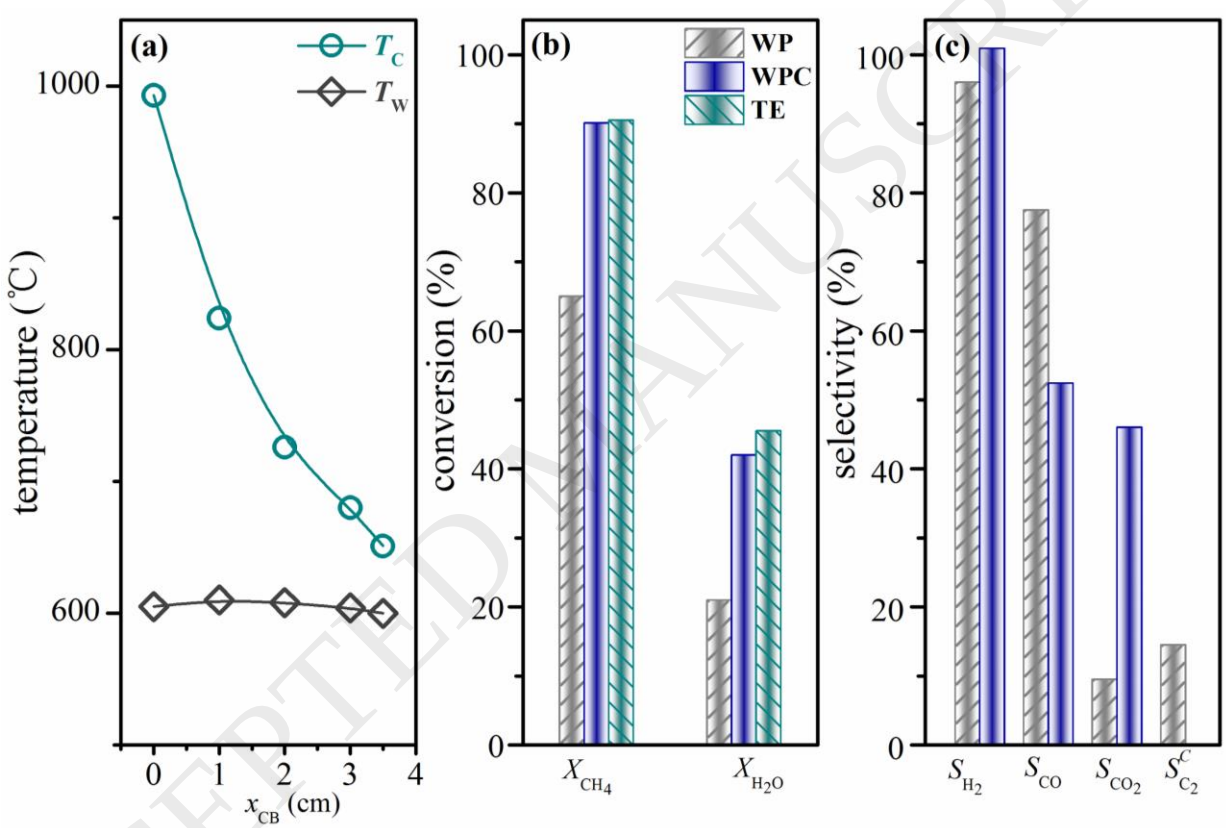

Figure 4. (a) Axial temperature profile of $Ni/CeO_2/Al_2O_3$ catalyst bed, and the comparison of SMR by approaches of warm plasma, warm plasma catalysis, and the thermodynamic equilibrium state in terms of (b) the conversion, and (c) the selectivity, under optimum conditions of *SEI*, S/C ratio, F_t, P, and GHSV of 110 kJ/mol, 3, 3 SLM, 246 W, 18000 $ml \cdot g^{-1} \cdot h^{-1}$, respectively.

In Figure 4b, compared with that of plasma alone process, the remarkable increase in the conversion of methane from 65 to 90% and water from 21 to 42% is observed, which approaches the thermo-

dynamic equilibrium state value at 651 ºC of the end temperature of catalyst bed. Apparently, the endothermic SMR reaction performs well at catalyst-bed zone (after plasma zone) with efficient utilization of the energy sourced from warm plasma, which is evidenced by this remarkable increase in methane conversion. The strong endothermicity of SMR accounts for the significant drop in catalyst-bed temperature, i.e., the higher temperature represents the faster reaction kinetics hence the much steeper drop in temperature (at the first 2 cm). Moreover, Figure 4c shows the decrease in CO selectivity from 77 to 52% and the increase in CO_2 selectivity from 10 to 46%. Hence, the changes in selectivity of CO and CO_2, is the evidence for the WGS (R2) over the catalyst. Clearly, at the catalyst bed zone the WGS is more promoted than the SMR. Inspiringly, the complete conversion of the C_2H_x (that was generated at plasma zone) occurs with the hydrogen selectivity rising from 96% to around 100% in Figure 4c.

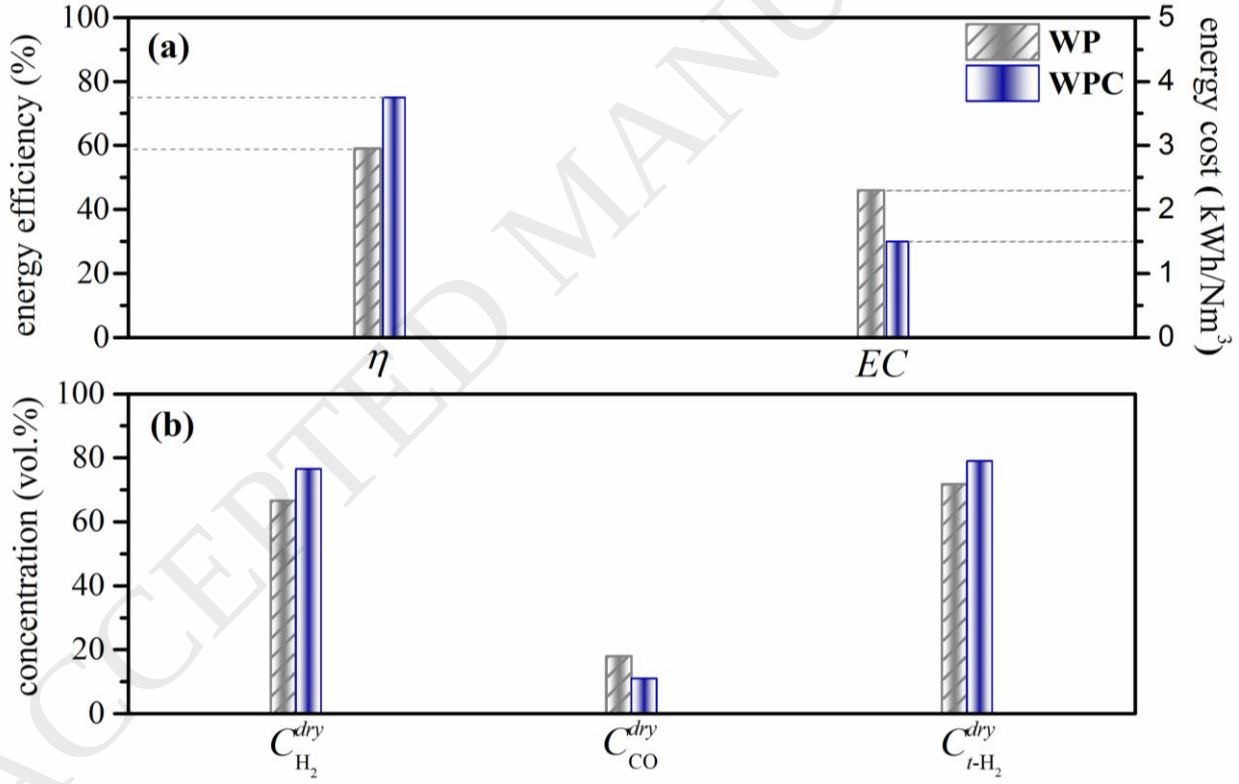

Figure 5. (a) Energy efficiency and energy cost, and (b) dry-basis concentration of H_2, CO, *t*-H_2 for SMR by approaches of warm plasma and warm plasma catalysis under the same conditions as Figure 4.

Figure 5a shows the energy efficiency (of methane to hydrogen) of 75% and the energy cost of 1.5 kWh/Nm^3 for warm plasma catalysis, compared to 59% and 2.3 kWh/Nm^3 for warm plasma. Figure 5b shows the dry concentration of H_2 (also *t*-H_2) up to 76% (79%) and CO down to 11% for SMR by warm plasma catalysis. The increase in H_2 (also *t*-H_2) concentration and the decrease in CO concentration arise from the remarkable increase in methane conversion in Figure 4b, thus the less remained methane, and the complete conversion of C_2H_x in Figure 4c.

3.3 Stability test and the characterization on catalysts

Figure S2 shows six hours stability test for warm plasma catalytic SMR. Methane conversion and water conversion keep steady at 90% and 42%, and the selectivity of CO, CO_2 and H_2 does at 52%, 46% and approximate 100%, respectively. The stability test manifests that warm plasma zone and Ni-based catalyst bed zone work well under the optimum conditions of Figure 4.

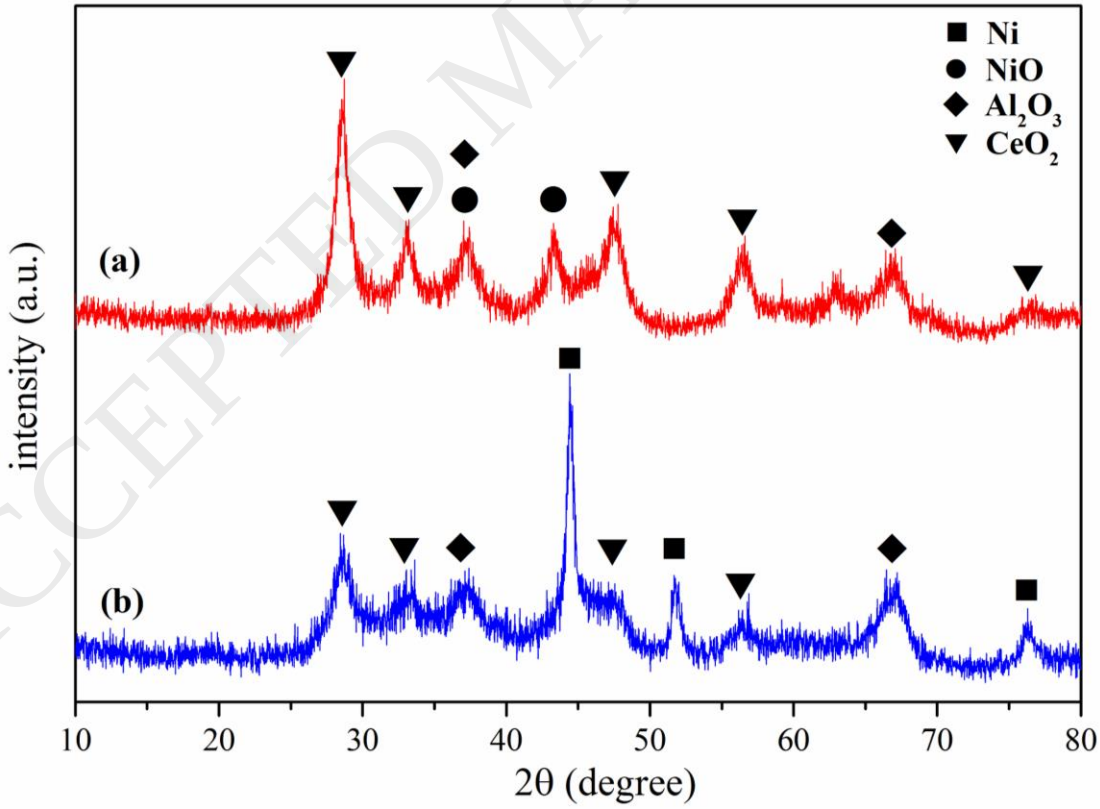

Figure 6. XRD measurements on (a) the fresh and (b) the used Ni/CeO_2/Al_2O_3 catalysts before and after six-hour stability test under the same conditions of Figure 4.

Figure 6 shows XRD spectra of the fresh and the used $Ni/CeO_2/Al_2O_3$ catalysts before and after six-hour stability test. The assigned peaks of Al_2O_3, CeO_2, NiO were observed for the fresh sample. For the used sample, the weaker peaks of CeO_2 appear, meanwhile the peaks of NiO disappear completely with the appearance of peaks of metallic Ni at 44.5° (strong), 51.9° and 76.4° (weak). It is evidence that Ni-based catalyst can be auto-reduced during the reaction, which allows no pre-reduction process [21]. Using Scherrer equation, the calculated Ni nanoparticles are around 17.2 nm in average size.

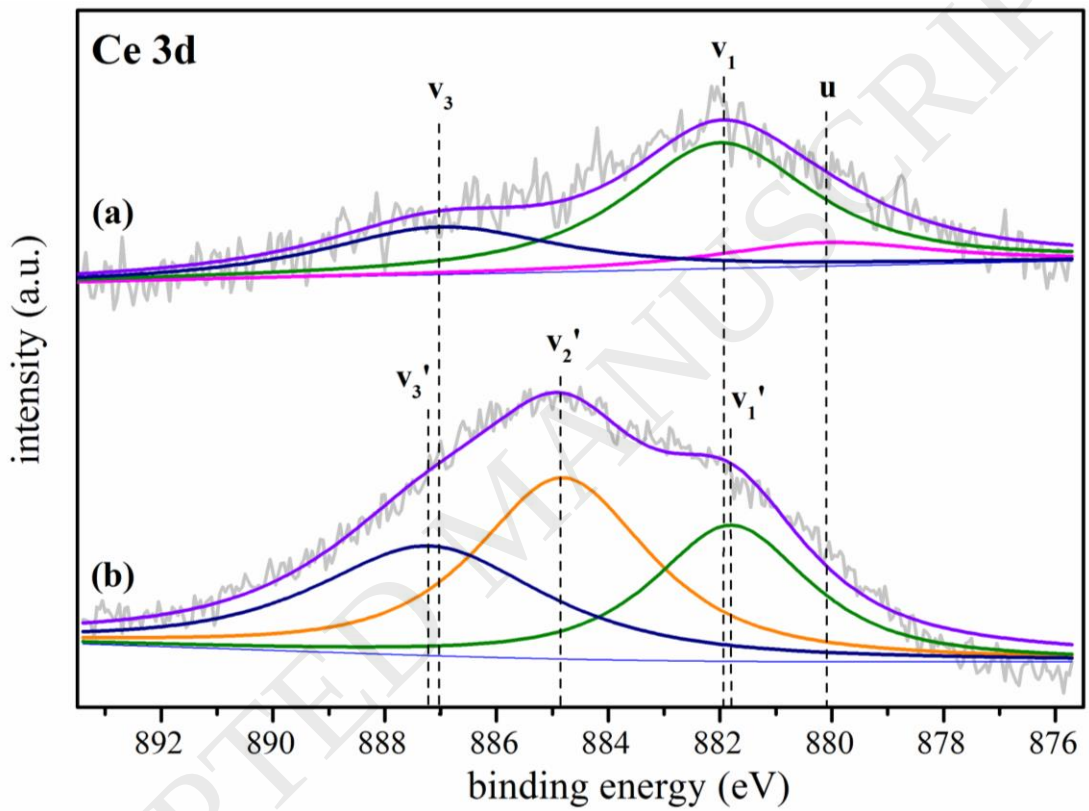

Figure 7. XPS spectra of Ce 3d for (a) the fresh and (b) the used $Ni/CeO_2/Al_2O_3$ catalysts before and after six-hour stability test under the same conditions of Figure 4.

Figure 7 shows XPS spectra of Ce 3d of the fresh and used catalyst samples. Three peaks are distinguished by the deconvolution of Ce 3d spectra for both samples. Consistent with literature [32], the peaks of Ce $3d_{3/2}$ are marked as u, and that of Ce $3d_{5/2}$ as v1, v_1', v_2',v_3 and v_3'. For the fresh sample, the peaks of v_1 (881.9 eV, $3d^94f^2$) and v_3 (887 eV, $3d^94f^1$) are assigned to Ce^{4+} and u (880.1 eV, $3d^94f^2$) to Ce^{3+}[32, 33]. For the used sample after the reaction, the peaks of v_1'(881.8 eV, $3d^94f^2$) and v_3'(887.2 eV,

$3d^94f^1$) are assigned to Ce^{4+}, and v_2'(884.9 eV, $3d^94f^1$) to Ce^{3+}[34]. During the reaction, the Ce^{4+} on the surface of catalysts can be easily reduced. Before the reaction a very small amount of Ce^{3+} (indicated by the weak peak u) appears in the fresh catalyst, while after the reaction a large amount of Ce^{3+} (stronger peak v_2') appears in the used catalyst, which is attributed to the reduction of Ce^{4+} to Ce^{3+} during the reaction. More interestingly, after the reaction, the remarkable increase in the amount of Ce^{3+} is consistent with and accounts for the decrease in the peak intensity of CeO_2 (representing Ce^{4+}) of XRD spectrum in Figure 6.

In Figure S3 EDS mapping is conducted on the fresh and used catalysts. It shows that the distribution of Ce and Ni elements on catalyst surface appears no obvious changes. It is quite consistent with the results of stability test, i.e., the conversion and the selectivity keep steady for six hours. Also it indicates the good stability of the reaction of warm plasma catalytic SMR.

3.4 Plasma-based approaches for SMR

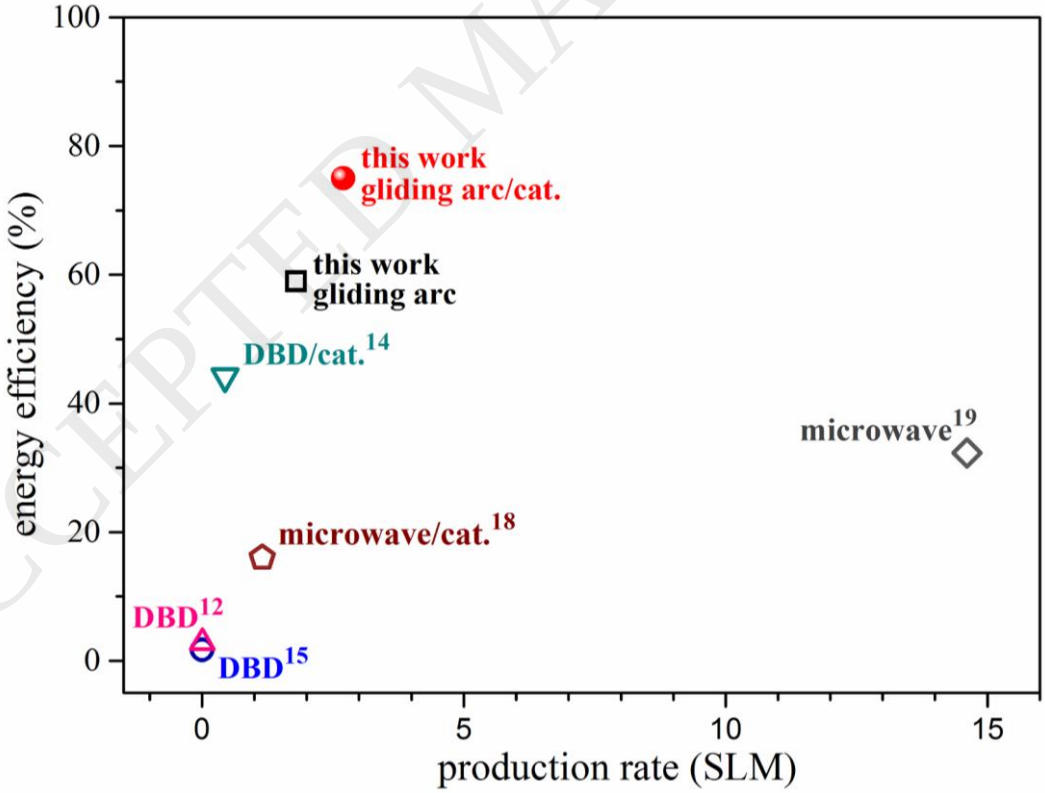

Figure 8. Energy efficiency with production rate of H_2 and CO for SMR reaction by various non-thermal plasma-based reforming approaches under conditions in Table 2.

In Figure 8 it shows the comparision among plasma-based approaches for SMR. Although total H_2 (t-H_2) is used anywhere in the present work, herein the term of the production rate of H_2 and CO is used for consistency with references. In general, warm plasmas possess much higher energy efficieny (also with larger conversion in Table 2) than cold plasmas. The energy efficiency of gliding arc plasma can be up to 35 times that of DBD (excluding DBD of literature [14] due to the calculation). The calculated energy efficiency of literature [14] excluded the extra heating (that was used), which needs to be informed. Worth noting is that, in this work warm plasma catalytic SMR is conducted, achieving high energy efficiency of 75% at large production rate of H_2 and CO of 2.7 SLM, which far exceeds the results of non-thermal plasma-based approaches for SMR for hydrogen production.

Table 2. Conditions and conversions for various non-thermal plasma-based approaches for SMR for hydrogen production.

Plasma	Catalyst	S/C	X_{CH_4}(%)	reference
gliding arc	$Ni/CeO_2/Al_2O_3$	3	90	this work
gliding arc		3	65	this work
DBD	Ni/Al_2O_3	2	46	[14]
DBD		0.25	19	[12]
DBD		1	4.8	[15]
microwave		3	95	[19]
microwave	Ni/Al_2O_3	3	80	[18]

CONCLUSIONS

In this work plasma catalytic SMR for distributed hydrogen production was conducted, for which warm plasma by gliding arc discharge initiates the reaction, followed by Ni-based ($Ni/CeO_2/Al_2O_3$) catalyst in a heat-insulated reactor without extra heating.

For plasma alone process, energy density *SEI* and S/C ratio contribute to the methane conversion due to the forward shift of chemical equilibrium, and inhibit the formation of C_2H_x resulting in the increase in the selectivity of H_2, CO, CO_2. Moreover, total flow rate F_t contributes to the methane conversion, however has no influence on the selectivity, indicating the identical reaction pathway (of methane reforming).

To efficiently utilize the heat and the active species sourced from the plasma zone, such a coupled process of warm plasma catalytic SMR is performed. For the plasma catalytic process, the methane conversion is further enhanced favorably with the complete disappearance of C_2H_x. The changes in selectivity of CO and CO_2 are the evidence for the WGS (R2) over the catalyst.

Warm plasma catalytic SMR was performed steady for six hours under optimum conditions of *SEI*, S/C ratio, F_t, and GHSV of 110 kJ/mol, 3, 3 SLM, 18000 $ml \cdot g^{-1} \cdot h^{-1}$, respectively. It achieved methane conversion of 90% at production rate of total H_2 (t-H_2) of 2.7 SLM. Compared with warm plasma alone process, the energy cost of warm plasma catalytic process reduces from 2.3 to 1.5 kWh/Nm^3, and the energy efficiency (of methane to t-H_2) from 59% to 75%.

XRD and XPS measurements were conducted on the catalysts before and after stability test, and it was observed that $Ni/CeO_2/Al_2O_3$ catalysts can be auto-reduced during the reaction.

References

[1] https://cafcp.org/sites/default/files/h2_station_list.pdf; https://www.californiahydrogen.org/wp-content/uploads/2017/10/1345-01-Fukumoto_FCE.pdf.

[2] B. Bej, N.C. Pradhan, S. Neogi, Production of hydrogen by steam reforming of methane over alumina supported nano-NiO/SiO_2 catalyst, Catalysis Today, 207 (2013) 28-35.

[3] C.-H. Kim, J.-Y. Han, H. Lim, K.-Y. Lee, S.-K. Ryi, Hydrogen production by steam methane reforming in membrane reactor equipped with Pd membrane deposited on NiO/YSZ/NiO multilayer-treated porous stainless steel, Journal of Membrane Science, 563 (2018) 75-82.

[4] Z. Xie, B. Yan, S. Kattel, J.H. Lee, S. Yao, Q. Wu, N. Rui, E. Gomez, Z. Liu, W. Xu, L. Zhang, J.G. Chen, Dry reforming of methane over CeO_2-supported Pt-Co catalysts with enhanced activity, Applied Catalysis B: Environmental, 236 (2018) 280-293.

[5] S.K. Cheah, L. Massin, M. Aouine, M.C. Steil, J. Fouletier, P. Gélin, Methane steam reforming in water deficient conditions on $Ir/Ce_{0.9}Gd_{0.1}O_{2-x}$ catalyst: Metal-support interactions and catalytic activity enhancement, Applied Catalysis B: Environmental, 234 (2018) 279-289.

[6] S.M. Sajjadi, M. Haghighi, Impregnation vs. sol-gel and sol-gel-plasma dispersion of nickel nanoparticles over Al_2O_3 employed in combined dry reforming and partial oxidation of greenhouse gases to syngas, International Journal of Hydrogen Energy, 43 (2018) 15014-15029.

[7] N. Edwards, S.R. Ellis, J.C. Frost, S.E. Golunski, A.N.J. van Keulen, N.G. Lindewald, J.G. Reinkingh, On-board hydrogen generation for transport applications: the HotSpot (TM) methanol processor, Journal of Power Sources, 71 (1998) 123-128.

[8] T. Aicher, J. Full, A. Schaadt, A portable fuel processor for hydrogen production from ethanol in a 250 W-el fuel cell system, International Journal of Hydrogen Energy, 34 (2009) 8006-8015.

[9] S.D. Angeli, G. Monteleone, A. Giaconia, A.A. Lemonidou, State-of-the-art catalysts for CH_4 steam reforming at low temperature, International Journal of Hydrogen Energy, 39 (2014) 1979-1997.

[10] M.A. Nieva, M.M. Villaverde, A. Monzón, T.F. Garetto, A.J. Marchi, Steam-methane reforming at low temperature on nickel-based catalysts, Chemical Engineering Journal, 235 (2014) 158-166.

[11] T. Nozaki, K. Okazaki, Non-thermal plasma catalysis of methane: Principles, energy efficiency, and applications, Catalysis Today, 211 (2013) 29-38.

[12] X. Zhang, B. Wang, Y. Liu, G. Xu, Conversion of Methane by Steam Reforming Using Dielectric-barrier Discharge, Chinese Journal of Chemical Engineering, 17 (2009) 625-629.

[13] A.M. Montoro-Damas, A. Gómez-Ramírez, A.R. Gonzalez-Elipe, J. Cotrino, Isotope labelling to study molecular fragmentation during the dielectric barrier discharge wet reforming of methane, Journal of Power Sources, 325 (2016) 501-505.

[14] Q. Liu, H. Zheng, R. Yang, G. Pan, Experimental study on chemical recuperation using hybrid dielectric barrier discharge-catalytic methane-steam reforming, Proceedings of the Institution of Mechanical Engineers, Part A: Journal of Power and Energy, 228 (2014) 451-461.

[15] J.-L. Liu, R. Snoeckx, M.S. Cha, Steam reforming of methane in a temperature-controlled dielectric barrier discharge reactor: the role of electroninduced chemistry versus thermochemistry, Journal of Physics D: Applied Physics, 51 (2018) 385201-338510.

[16] M.-w. Li, G.-h. Xu, Y.-l. Tian, L. Chen, H.-f. Fu, Carbon Dioxide Reforming of Methane Using DC Corona Discharge Plasma Reaction, The Journal of Physical Chemistry A, 108 (2004) 1687-1693.

[17] D. Czylkowski, B. Hrycak, M. Jasiński, M. Dors, J. Mizeraczyk, Microwave plasma-based method of hydrogen production via combined steam reforming of methane, Energy, 113 (2016) 653-661.

[18] Y.-F. Wang, C.-H. Tsai, W.-Y. Chang, Y.-M. Kuo, Methane steam reforming for producing hydrogen in an atmospheric-pressure microwave plasma reactor, International Journal of Hydrogen Energy, 35 (2010) 135-140.

[19] D.H. Choi, S.M. Chun, S.H. Ma, Y.C. Hong, Production of hydrogen-rich syngas from methane reforming by steam microwave plasma, Journal of Industrial and Engineering Chemistry, 34 (2016) 286-291.

[20] K. Li, J.-L. Liu, X.-S. Li, X.-B. Zhu, A.-M. Zhu, Post-plasma catalytic oxidative CO_2 reforming of methane over Ni-based catalysts, Catalysis Today, 256 (2015) 96-101.

[21] K. Li, J.-L. Liu, X.-S. Li, X. Zhu, A.-M. Zhu, Warm plasma catalytic reforming of biogas in a heat-insulated reactor: Dramatic energy efficiency and catalyst auto-reduction, Chemical Engineering Journal, 288 (2016) 671-679.

[22] J.-L. Liu, Z. Li, J.-H. Liu, K. Li, H.-Y. Lian, X.-S. Li, X. Zhu, A.-M. Zhu, Warm-plasma catalytic reduction of CO_2 with CH_4, Catalysis Today, (2018) doi: 10.1016/j.cattod.2018.1005.1046.

[23] Y.N. Chun, Y.C. Yang, K. Yoshikawa, Hydrogen generation from biogas reforming using a gliding arc plasma-catalyst reformer, Catalysis Today, 148 (2009) 283-289.

[24] N. Rueangjitt, T. Sreethawong, S. Chavadej, H. Sekiguchi, Plasma-catalytic reforming of methane in AC microsized gliding arc discharge: Effects of input power, reactor thickness, and catalyst existence, Chemical Engineering Journal, 155 (2009) 874-880.

[25] F. Zhu, H. Zhang, X. Yan, J. Yan, M. Ni, X. Li, X. Tu, Plasma-catalytic reforming of CO_2-rich biogas over Ni/γ-Al_2O_3 catalysts in a rotating gliding arc reactor, Fuel, 199 (2017) 430-437.

[26] K. Pornmai, S. Suvachitanont, S. Chavadej, Reforming of CO_2-containing natural gas with steam in AC gliding arc discharge for hydrogen production, International Journal of Green Energy, 15 (2018) 441-453.

[27] B. Li, Z. Xu, F. Jing, S. Luo, N. Wang, W. Chu, Improvement of catalytic stability for CO_2 reforming of methane by copper promoted Ni-based catalyst derived from layered-double hydroxides, Journal of Energy Chemistry, 25 (2016) 1078-1085.

[28] F. Wang, B. Han, L. Zhang, L. Xu, H. Yu, W. Shi, CO2 reforming with methane over small-sized Ni@SiO_2 catalysts with unique features of sintering-free and low carbon, Applied Catalysis B: Environmental, 235 (2018) 26-35.

[29] E.-h. Yang, Y.S. Noh, G.H. Hong, D.J. Moon, Combined steam and CO_2 reforming of methane over $La_{1-x}Sr_xNiO_3$ perovskite oxides, Catalysis Today, 299 (2018) 242-250.

[30] H.-Y. Lian, X.-S. Li, J.-L. Liu, X. Zhu, A.-M. Zhu, Oxidative pyrolysis reforming of methanol in warm plasma for an on-board hydrogen production, International Journal of Hydrogen Energy, 42 (2017) 13617-13624.

[31] W. Piavis, S. Turn, An experimental investigation of reverse vortex flow plasma reforming of methane, International Journal of Hydrogen Energy, 37 (2012) 17078-17092.

[32] X. Liao, Y. Zhang, M. Hill, X. Xia, Y. Zhao, Z. Jiang, Highly efficient Ni/CeO_2 catalyst for the liquid phase hydrogenation of maleic anhydride, Applied Catalysis A: General, 488 (2014) 256-264.

[33] A. Löfberg, J. Guerrero-Caballero, T. Kane, A. Rubbens, L. Jalowiecki-Duhamel, Ni/CeO_2 based catalysts as oxygen vectors for the chemical looping dry reforming of methane for syngas production, Applied Catalysis B: Environmental, 212 (2017) 159-174.

[34] L.-Y. Lin, H. Bai, Promotional effects of manganese on the structure and activity of Ce–Al–Si based catalysts for low-temperature oxidation of acetone, Chemical Engineering Journal, 291 (2016) 94-105.

ACKNOWLEDGMENT

This work is supported by National Natural Science Foundation of China (11705019).

Additional information

Supporting Information.
Additional data, Figures S1-S3. The Supporting Information is available free of charge via the Internet at